Aalborg Universitet

Voltage Modulated Direct Power Control for a Weak Grid-Connected Voltage Source Inverters

Yonghao Gui, *Member, IEEE*, Xiongfei Wang, *Senior Member, IEEE*, Heng Wu, *Student Member, IEEE*, and Frede Blaabjerg, *Fellow, IEEE*.

Abstract—In this paper, we design a voltage modulated direct power control (VM-DPC) for a three-phase voltage source inverter (VSI) connected to a weak grid, where the PLL system may make the system unstable if the conventional vector current control (VCC) method is applied. Compared with the conventional VCC method, the main advantage of the proposed VM-DPC method is that the PLL system is eliminated. Moreover, in order to inject the rated real power to the weak grid, the VSI system should generate some certain amount of reactive power as well. An eigenvalues based analysis shows the system with the proposed method tracks its desired dynamics in the certain operating range. Both simulation and experimental results match the theoretical expectations closely.

Index Terms—Voltage source inverter, voltage modulated direct power control (VM-DPC), vector current controller, weak grid, stable system.

I. INTRODUCTION

VOLTAGE source converters (VSCs) are widely used in the application of smart grid, flexible AC transmission systems, and renewable energy sources (*e.g.,* wind and solar) in the modern power grids [1]–[7]. One of the key devices in VSCs is grid-connected voltage source inverter (VSI), which is normally controlled as a current source injecting current into the grid. For grid-connected VSIs, the conventional vector current control strategy is typically used to provide satisfactory control performance [8]. However, it has been reported that a weak grid-connected VSI with the standard vector current control strategy suffers from stability and performance issues [9]–[12]. In addition, with the increasing penetration of renewable energy resources in modern power grids, it becomes more and more important to sustain stability and high power quality induced by grid-connected VSIs [13].

A widely used control scheme for VSIs is the vector current control, where the phase-locked loop (PLL) is used for the purpose of grid synchronization [14]. In recent years, the adverse impact of the PLL on the small-signal stability of VSIs have been reported. It is found out that the PLL may deteriorate the stability of VSIs by introducing the negative incremental resistance at low frequencies [15]–[17]. The frequency coupling dynamics of VSIs introduced by the PLL have also been explicitly revealed in [18]. The frequency range

(*Corresponding Author: Xiongfei Wang.*)
Y. Gui was with the Dept. of Energy Technology, Aalborg University, and is now with Automation & Control Section at the Dept. of Electronic Systems, Aalborg University, 9220 Aalborg, Denmark. (e-mail: yg@es.aau.dk)
X. Wang, H. Wu, and F. Blaabjerg are with the Dept. of Energy Technology, Aalborg University, 9220 Aalborg, Denmark. (e-mail: xwa@et.aau.dk; hew@et.aau.dk; fbl@et.aau.dk).

of the negative resistance is determined by the bandwidth of the PLL. Therefore, the low bandwidth PLL is usually adopted in order to improve the stability robustness of VSIs, which jeopardizes the dynamic performance of the system significantly. Moreover, even though the PLL is designed with a very low bandwidth, it is still very difficult for VSIs to remain stable under the very weak grid condition, in which the grid impedance is approaching 1.3 pu [19]. Recently, *Wang* and *Blaabjerg* summarized the harmonic stability caused by the grid-connected VSIs in modern power grids [20], where the small-signal dynamics of VSIs tend to introduce a negative damping, which may be in different frequency ranges, depending on both the specific controllers of the converters and power system conditions [19]–[23]. Therefore, in order to guarantee stable operation of VSIs under the weak grid condition, the control strategy without the PLL is needed.

Another control method, direct power control (DPC), has been researched for grid-connected VSIs to control the instantaneous real and reactive powers directly without using neither inner-loop current regulator nor PLL system [24], [25]. However, these methods have a main disadvantage as a variable switching frequency based on the switching state, which results in an unexpected broadband harmonic spectrum, *i.e.,* it is not easy to design a line filter properly. To achieve a constant switching frequency, various DPC strategies have been proposed. Some of them are using space vector modulation [25], [26], or calculating the required converter voltage vector in each switching period [27], [28]. Moreover, with the consideration of the robustness, a sliding mode control is applied to the DPC method in order to guarantee a fast tracking performance of the real and reactive powers [29], and a passivity-based control via DPC is proposed by considering the system's intrinsic dissipative nature [30]. However, there are still undesirable ripples in both real and reactive powers. One of the optimal control algorithms, model predictive control (MPC)-DPC, has been designed by considering the multivariable case, nonlinearities, and system constraints in an intuitive way [31]–[35]. In every sampling period, MPC-DPC selects voltage vector sequence and calculates the duty cycles. MPC-DPC provides a constant switching frequency as well. However, it may incur additional computational burden.

Recently, *Gui et al.* introduced a grid voltage modulated-DPC (GVM-DPC), which solves the main disadvantage of the DPC method, the steady-state performance [36], [37]. It may be easily designed and analyzed for the grid-connected VSIs through various linear control techniques since a linear time-invariant (LTI) system is obtained based on the GVM-DPC
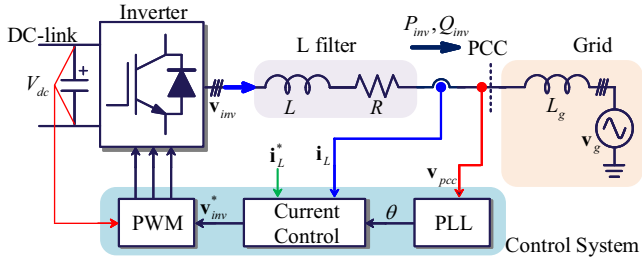
Fig. 1. Simplified vector current control structure of a single-line diagram three-phase voltage source inverter connected to a weak grid.

concept [38], [39]. However, for the GVM-DPC method, it starts from a strong assumption that it needs a non-distorted grid voltage. Consequently, in this paper, we will show how to use that method in a weak grid, where the point of common coupling (PCC) voltage is affected by the injected currents from VSIs.

In this paper, we design a voltage modulated direct power control (VM-DPC) strategy for the three-phase VSI connected to a weak grid, where the PLL system may make the system unstable as discussed before. The main advantage of the proposed method is that the PLL system is eliminated. In order to use the concept of the GVM-DPC, we use a band-pass-filter (BPF) for a weak grid connected VSI system to apply the similar concept. In addition, in order to inject the rated real power to the weak grid, the system should generate some certain amount of reactive power to support the voltages at the PCC as well. Finally, a comprehensive analysis is presented to show the improvement of the stability of the system with the proposed method.

The rest of the paper is organized as follows. Section II presents the system modeling of the grid-connected VSI based on the DPC model and the GVM-DPC based on BPF. In Section III, we show a stability analysis for the whole system including the BPF with consideration of the parameter variations. Section IV shows the simulation results using MAT-LAB/Simulink, Simscape Power Systems and experimental test using a 15-kW-inverter system. Finally, the conclusions of this work are given in Section V.

II. MODELING OF GRID-CONNECTED VOLTAGE SOURCE INVERTERS

In this Section, at first, a DPC modeling of VSC is briefly introduced. Then, a VM-DPC is proposed for the VSI system to make it to become an LTI system.

A. Modeling

Fig. 1 shows a simplified single-line diagram of a two-level VSI connected to a weak grid through an L-filter. In this study, we assume that a stiff dc source (V_{dc}) is connected to the dc-side of the inverter, *e.g.,* a dc-dc converter in a PV application or a rectifier in wind application. Hence, the dynamic from the dc input is not considered in this paper. In addition, a grid impedance (L_g) is considered at the grid-side. Normally, the voltages at the PCC, ($\mathbf{v}_{pcc}$), are measured to synchronize the VSI with the grid through the PLL. For the current control,

either the proportional+integral (PI) controller in the dq–frame or the proportional+resonant (PR) controller in the $\alpha\beta$–frame could be applied to generate the voltage references for the PWM. In this study, we only compare the PI controller in the dq–frame with the proposed method.

The dynamic equations consisting of the output voltages of the VSI, the voltages at the PCC, and the output currents can be expressed as follows:

$$
\begin{aligned}
L\frac{di_{L,a}}{dt} &= -Ri_{L,a} + v_{inv,a} - v_{pcc,a}, \\
L\frac{di_{L,b}}{dt} &= -Ri_{L,b} + v_{inv,b} - v_{pcc,b}, \\
L\frac{di_{L,c}}{dt} &= -Ri_{L,c} + v_{inv,c} - v_{pcc,c},
\end{aligned}
\tag{1}
$$

where

$$
\begin{aligned}
v_{pcc,a} &= L_g\frac{di_{L,a}}{dt} + v_{g,a}, \\
v_{pcc,b} &= L_g\frac{di_{L,b}}{dt} + v_{g,b}, \\
v_{pcc,c} &= L_g\frac{di_{L,c}}{dt} + v_{g,c},
\end{aligned}
\tag{2}
$$

where $i_{L,abc}$, v_{gabc}, $v_{inv,abc}$ are the output current, the grid voltage, and the output voltage of the VSI in the abc frame, respectively. L and R are the filter inductance and resistance, respectively. Based on a balanced grid voltage condition, the dynamic equations in (1) can be transformed into the stationary reference frame by using Clark transformation as follows:

$$
\begin{aligned}
L\frac{di_{L,\alpha}}{dt} &= -Ri_{L,\alpha} + v_{inv,\alpha} - v_{pcc,\alpha}, \\
L\frac{di_{L,\beta}}{dt} &= -Ri_{L,\beta} + v_{inv,\beta} - v_{pcc,\beta},
\end{aligned}
\tag{3}
$$

where $i_{L,\alpha\beta}$, $v_{pcc,\alpha\beta}$, and $v_{inv,\alpha\beta}$ indicate the output currents, the voltages at the PCC, and the inverter output voltages in the $\alpha\beta$–frame, respectively.

In (2), we observe that the voltages at the PCC are affected by the injected currents. However, the GVM-DPC proposed in [37] starts from a non-distorted voltage. Consequently, if we only consider a fundamental frequency of the voltage at PCC, then the injected currents will be the fundamental ones as well. It is acceptable since the fundamental of real and reactive powers are expected to be injected in the grid from the grid-side. Hence, we will use a band-pass-filter (BPF) to obtain the fundamental component of the measured PCC voltages.

$$
v_{pcc,\alpha\beta_f} = G_{bpf} * v_{pcc,\alpha\beta},
\tag{4}
$$

where G_{bpf} is the transfer function of the BPF and $v_{pcc,\alpha\beta_f}$ is the fundamental component of the measured voltages at the PCC. Consequently, we can obtain the instantaneous fundamental real and reactive powers injected from VSI to the grid in the stationary reference frame as follows [40], [41]:

$$
\begin{aligned}
P_f &= \frac{3}{2}(v_{pcc,\alpha_f}i_{L,\alpha} + v_{pcc,\beta_f}i_{L,\beta}), \\
Q_f &= \frac{3}{2}(v_{pcc,\beta_f}i_{L,\alpha} - v_{pcc,\alpha_f}i_{L,\beta}),
\end{aligned}
\tag{5}
$$

where P_f and Q_f indicate the fundamental component of the instantaneous real and reactive powers injected into the grid,

respectively. Differentiating (5) with respect to time, we can obtain the dynamics of the instantaneous real and reactive powers as follows:

$$
\begin{aligned}
\frac{dP_f}{dt} &= \frac{3}{2}\left(i_{L,\alpha}\frac{dv_{pcc,\alpha_f}}{dt} + v_{pcc,\alpha_f}\frac{di_{L,\alpha}}{dt}\right.\\
&\qquad\left. + i_{L,\beta}\frac{dv_{pcc,\beta_f}}{dt} + v_{pcc,\beta_f}\frac{di_{L,\beta}}{dt}\right),\\
\frac{dQ_f}{dt} &= \frac{3}{2}\left(i_{L,\alpha}\frac{dv_{pcc,\beta_f}}{dt} + v_{pcc,\beta_f}\frac{di_{L,\alpha}}{dt}\right.\\
&\qquad\left. - i_{L,\beta}\frac{dv_{pcc,\alpha_f}}{dt} - v_{pcc,\alpha_f}\frac{di_{L,\beta}}{dt}\right).
\end{aligned}
\tag{6}
$$

Since $\mathbf{v}_{pcc}$ is a fundamental part of the PCC voltages, we can obtain the following relationship such as

$$
\begin{aligned}
v_{pcc,\alpha_f} &= V_{pcc_f}\cos(\omega_f t),\\
v_{pcc,\beta_f} &= V_{pcc_f}\sin(\omega_f t),
\end{aligned}
\tag{7}
$$

where V_{pcc_f} is the magnitude of the fundamental PCC voltages, $V_{pcc_f} = \sqrt{v_{pcc,\alpha}^2 + v_{pcc,\beta}^2}$. ω_f is the angular frequency of the fundamental PCC voltages and $\omega_f = 2\pi f$, and f is the fundamental frequency of the grid voltage. Differentiating (7) with respect to time, we can obtain instantaneous fundamental PCC voltage dynamics as follows:

$$
\begin{aligned}
\frac{dv_{pcc,\alpha_f}}{dt} &= -\omega_f V_{pcc_f}\sin(\omega_f t) = -\omega_f v_{pcc,\beta_f},\\
\frac{dv_{pcc,\beta_f}}{dt} &= \omega_f V_{pcc_f}\cos(\omega_f t) = \omega_f v_{pcc,\alpha_f}.
\end{aligned}
\tag{8}
$$

Substituting (3) and (8) into (6), the state-space models of the fundamental real and reactive powers are generated as follows [29]:

$$
\begin{aligned}
\frac{dP_f}{dt} &= -\frac{R}{L}P_f - \omega_f Q_f\\
&\quad + \frac{3}{2L}\left(v_{pcc,\alpha_f}v_{inv,\alpha} + v_{pcc,\beta_f}v_{inv,\beta} - V_{pcc_f}^2\right),\\
\frac{dQ_f}{dt} &= \omega_f P_f - \frac{R}{L}Q_f + \frac{3}{2L}\left(v_{pcc,\beta_f}v_{inv,\alpha} - v_{pcc,\alpha_f}v_{inv,\beta}\right).
\end{aligned}
\tag{9}
$$

Note that the dynamics of instantaneous real and reactive powers in (9) are a multi-input-multi-output (MIMO) system, where $v_{inv,\alpha}$ and $v_{inv,\beta}$ are the control inputs, and P_f and Q_f are the outputs. Moreover, notice that the system is a time-varying one since both control inputs are multiplied by the grid voltages.

B. Controller Design

To simplify the dynamics in (9), we define a VM-DPC input as follows:

$$
\begin{aligned}
u_P &:= v_{pcc,\alpha_f}v_{inv,\alpha} + v_{pcc,\beta_f}v_{inv,\beta} - V_{pcc_f}^2,\\
u_Q &:= v_{pcc,\beta_f}v_{inv,\alpha} - v_{pcc,\alpha_f}v_{inv,\beta},
\end{aligned}
\tag{10}
$$

where u_P and u_Q are the new control inputs, which will be designed. With the new control inputs defined in (10),

the dynamics of the real and reactive powers in (9) can be rewritten as follows:

$$
\begin{aligned}
\frac{dP_f}{dt} &= -\frac{R}{L}P_f - \omega Q_f + \frac{3}{2L}u_P,\\
\frac{dQ_f}{dt} &= \omega P_f - \frac{R}{L}Q_f + \frac{3}{2L}u_Q.
\end{aligned}
\tag{11}
$$

Note that the dynamics of the real and reactive powers in (11) are changed into a linear time-invariant (LTI) MIMO system with the coupling states, which has a simple structure like the model of d–q axes currents of VSI.

Let's define the errors of the real and reactive powers as follows:

$$
\begin{aligned}
e_P &:= P^* - P_f,\\
e_Q &:= Q^* - Q_f,
\end{aligned}
\tag{12}
$$

where P^* and Q^* are the references of the real and reactive powers, respectively. In order to cancel the coupling terms in (11), a simple controller consisting of feedforward and PI feedback is designed as follows:

$$
\begin{aligned}
u_P &= \frac{2L\omega_f}{3}Q_f + K_{P,p}e_P + K_{P,i}\int_0^t e_P(\tau)d\tau,,\\
u_Q &= -\frac{2L\omega_f}{3}P_f + K_{Q,p}e_Q + K_{Q,i}\int_0^t e_Q(\tau)d\tau,
\end{aligned}
\tag{13}
$$

where $K_{P,p}$, $K_{P,i}$, $K_{Q,p}$, and $K_{Q,i}$ are the PI controller gains. Substituting (13) into (11), the error dynamics of real and reactive powers could be obtained as

$$
\begin{aligned}
\dot{e}_P &= -(K_{P,p} + \frac{R}{L})e_P - K_{P,i}\int_0^t e_P(\tau)d\tau,\\
\dot{e}_Q &= -(K_{Q,p} + \frac{R}{L})e_Q - K_{Q,i}\int_0^t e_Q(\tau)d\tau.
\end{aligned}
\tag{14}
$$

Roughly, the closed-loop system with the proposed method is exponentially stable in the operating range if the PI controller gains are positive. Finally, the original control inputs, $v_{inv,\alpha}$ and $v_{inv,\beta}$, could be calculated by means of (10) as follows:

$$
\begin{aligned}
v_{inv,\alpha} &= \frac{v_{pcc,\alpha_f}u_P + v_{pcc,\beta_f}u_Q + V_{pcc_f}^2 v_{pcc,\alpha_f}}{V_{pcc_f}^2},\\
v_{inv,\beta} &= \frac{v_{pcc,\beta_f}u_P - v_{pcc,\alpha_f}u_Q + V_{pcc_f}^2 v_{pcc,\beta_f}}{V_{pcc_f}^2}.
\end{aligned}
\tag{15}
$$

The block diagram of the proposed method is shown in Fig. 2.

III. STABILITY ANALYSIS

In this section, we investigate the eigenvalues of the error dynamics with the proposed method. Based on such eigenvalues, we analyze the stability of the weak grid-connected VSI.

At first, let us define the transfer function of the BPF used in this study as follows:

$$
G_{bpf} = \frac{2\omega_c s}{s^2 + 2\omega_c s + \omega_0^2},
\tag{16}
$$

where $\omega_c = \zeta\omega_0$ is the resonance bandwidth, ω_0 is the resonance frequency, and ζ is damping ratio. To obtain the state-space model of the BPF, we define the new state $x_{bpf} \in \mathbb{R}^4$,
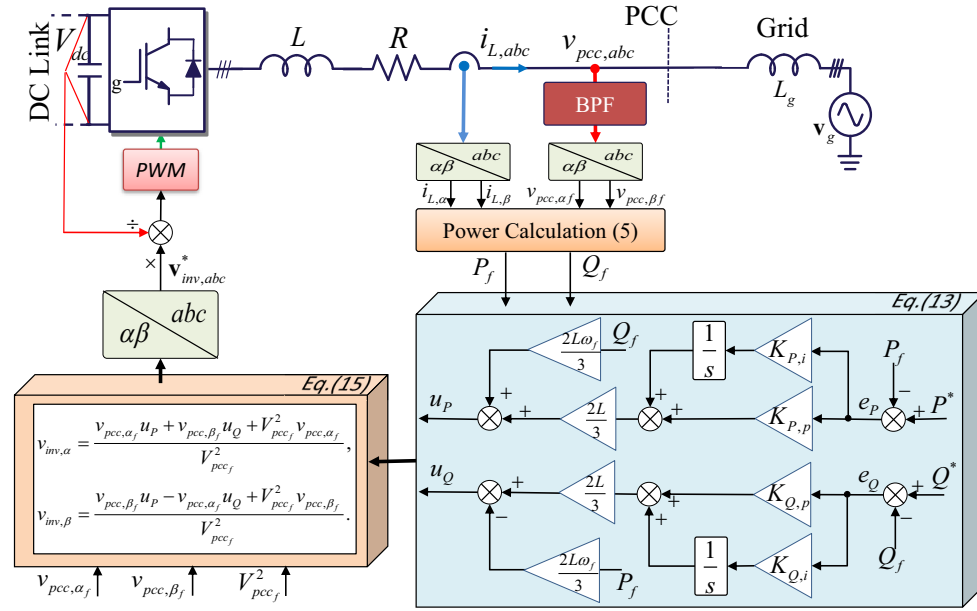
Fig. 2. Block diagram the proposed method for the weak grid-connected voltage source inverter.

the control inputs $u_{bpf} = \begin{bmatrix} v_{pcc,\alpha}, & v_{pcc,\beta} \end{bmatrix}^T$, and the output $y_{bpf} = \begin{bmatrix} v_{pcc,\alpha_f}, & v_{pcc,\beta_f} \end{bmatrix}^T$, then the state-space model of the BPF can be obtained as follows:

$$\dot{x}_{bpf} = \begin{bmatrix} -2\omega_c & -\omega_0^2 & 0 & 0 \\ 1 & 0 & 0 & 0 \\ 0 & 0 & -2\omega_c & -\omega_0^2 \\ 0 & 0 & 1 & 0 \end{bmatrix} x_{bpf} + \begin{bmatrix} 1 & 0 \\ 0 & 0 \\ 0 & 1 \\ 0 & 0 \end{bmatrix} u_{bpf},$$

$$y_{bpf} = \begin{bmatrix} 2\omega_c & 0 & 0 & 0 \\ 0 & 0 & 2\omega_c & 0 \end{bmatrix} x_{bpf}.$$

$$(17)$$

To simplify the analysis, we use the proportional controller instead of the PI controller in (13). In order to obtain the closed-loop system, we substitute (15) and (17) into (3). Finally, we can obtain the closed-loop system as

$$\dot{x} = A(x)x + Bu, \qquad (18)$$

where $x = \begin{bmatrix} i_\alpha, & i_\beta, & x_{bpf} \end{bmatrix}^T \in \mathbb{R}^6$ and $u = \begin{bmatrix} v_{g,\alpha}, & v_{g,\beta} \end{bmatrix}^T \in \mathbb{R}^2$. Moreover, A and B are listed in (19) at the bottom of the paper. Since the state variables are ac signals, the error dynamics is used to consider its tracking

behavior, which has only one equilibrium point at the origin. We assume that there exists signal x^d to satisfy the following relationship:

$$\dot{x}^d = A(x^d)x^d + Bu, \qquad (20)$$

where $x^d = \begin{bmatrix} i_\alpha^d, & i_\beta^d, & x_{bpf}^d \end{bmatrix}^T \in \mathbb{R}^6$. The superscript "$d$" indicates the desired value. The assumption in (20) is acceptable in this study, since we consider that the system dynamics are sufficiently smooth in an open connected set.

It should be noted that the proposed method stabilizes the system exponentially based on (14), i.e., P_f and Q_f converge to their references exponentially. Hence, in this study, we do not consider the dynamics of $V_{pcc_f}^2$ in (19), i.e., $V_{pcc_f}^2 \approx V_{pcc_f}^{d2}$. It is acceptable since $V_{pcc_f}^2$ is a dc value and has a slow dynamics compared to the currents. If we define an error as follows:

$$e = x^d - x, \qquad (21)$$

then, the error dynamics could be obtained as

$$\dot{e} = \dot{x}^d - \dot{x} = A(x^d)e \qquad (22)$$

$$A(x) = \begin{bmatrix} \frac{-R-\frac{3}{2}K_{P,p}}{L+L_g} & -\frac{L\omega_f}{L+L_g} & \frac{2\omega_c}{L+L_g}\left(1+\frac{K_{P,p}P^*}{V_{pcc_f}^2}\right) & 0 & \frac{2\omega_c}{L+L_g}\left(\frac{K_{P,p}Q^*}{V_{pcc_f}^2}\right) & 0 \\ \frac{L\omega_f}{L+L_g} & \frac{-R-\frac{3}{2}K_{Q,p}}{L+L_g} & -\frac{2\omega_c}{L+L_g}\left(\frac{K_{Q,p}Q^*}{V_{pcc_f}^2}\right) & 0 & \frac{2\omega_c}{L+L_g}\left(1+\frac{K_{P,p}P^*}{V_{pcc_f}^2}\right) & 0 \\ \frac{-R-\frac{3}{2}K_{P,p}}{L+L_g}L_g & -\frac{L\omega_f}{L+L_g}L_g & \frac{2\omega_c(1+K_{P,p}P^*/V_{pcc_f}^2)}{L+L_g}L_g - 2\omega_c & -\omega_0^2 & \frac{2\omega_c K_{Q,p}Q^*/V_{pcc_f}^2}{L+L_g}L_g & 0 \\ 0 & 0 & 1 & 0 & 0 & 0 \\ \frac{L\omega_f}{L+L_g}L_g & \frac{-R-\frac{3}{2}K_{Q,p}}{L+L_g}L_g & -\frac{2\omega_c K_{Q,p}Q^*/V_{pcc_f}^2}{L+L_g}L_g & 0 & \frac{2\omega_c(1+K_{P,p}P^*/V_{pcc_f}^2)}{L+L_g}L_g - 2\omega_c & -\omega_0^2 \\ 0 & 0 & 0 & 0 & 1 & 0 \end{bmatrix},$$

$$B = \begin{bmatrix} -1 & 0 & 1-L_g & 0 & 0 & 0 \\ 0 & -1 & 0 & 0 & 1-L_g & 0 \end{bmatrix}^T.$$

$$(19)$$

where $A(x^d)$ is listed in (23) at the bottom of the paper.

Consequently, we could consider $V_{pcc,f}$ based on a phasor diagram, as shown in Fig. 3. It should be noted that upper-case letters are used for magnitude and lower-case letters are used for instantaneous variables in this study. We define V_{pcc}, V_g, and I_L, being the magnitude of v_{pcc}, v_g, and i_L, respectively. From Fig. 3, V_{pcc}^d has a relationship between V_g and I_L^d such as

$$V_{pcc}^{d2} = V_g^2 - (\omega_f L_g I_L^d)^2. \qquad (24)$$

If we consider the only real power, then we can obtain the following relationship such as

$$I_L^d = \frac{2}{3}\frac{P^d}{V_{pcc}}, \qquad (25)$$

Substituting (25) into (24), V_{pcc} can be obtained as

$$V_{pcc}^{d2} = \frac{V_g^2}{2} \pm \sqrt{\frac{V_g^4}{4} - (\frac{2}{3}\omega_f L_g P^d)^2}. \qquad (26)$$

When $P^d = 0$, V_{pcc}^d should be equal to V_g. Hence, it should be '+' in (26). Notice that, $\frac{V_g^4}{4} - (\frac{2}{3}\omega_f L_g P^d)^2$ should be larger than zero since V_{pcc}^{d2} should have real value. That means the inverter has a maximum real power injecting to the weak grid, which has been discussed in [42].

To analyze the weak-grid connected VSI, we assume that the capacity of the VSI is 3.5 kW. Consequently, we obtain $L_g = 22$ mH when $SCR = 1.5$ and the root mean square (RMS) of the grid voltage, $V_{ga,rms}$, is 110 V. In addition, the BPF is designed as follows: $\omega_0 = 2\pi f$ and $\zeta = 0.707$. Fig. 4 shows the eigenvalues of the closed-loop system in (22) when the real power increases from $P^d = 0$ to $P^d = 2.45$ kW. In this case, we fix $K_{P,p} = K_{Q,p} = 20$. We can observe that the eigenvalues of the closed-loop system move to the right-half-plane when we increase of the real power.

To inject the rated real power to the weak grid, the reactive power should generate to compensate the voltage at the PCC [42]. Consequently, (26) is changed into relationship in (27) based on the phasor diagram, as shown in Fig. 5.

$$V_{pcc}^{d2} = \frac{V_g^2 + \frac{4}{3}\omega_f L_g Q^d}{2}$$
$$+ \sqrt{\frac{(V_g^2 + \frac{4}{3}\omega_f L_g Q^d)^2}{4} - (\frac{2}{3}\omega_f L_g)^2(P^{d2} + Q^{d2})}. \qquad (27)$$
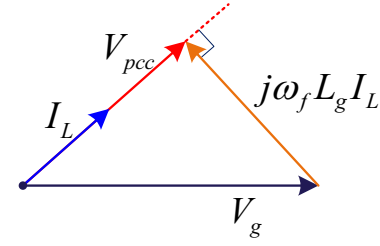
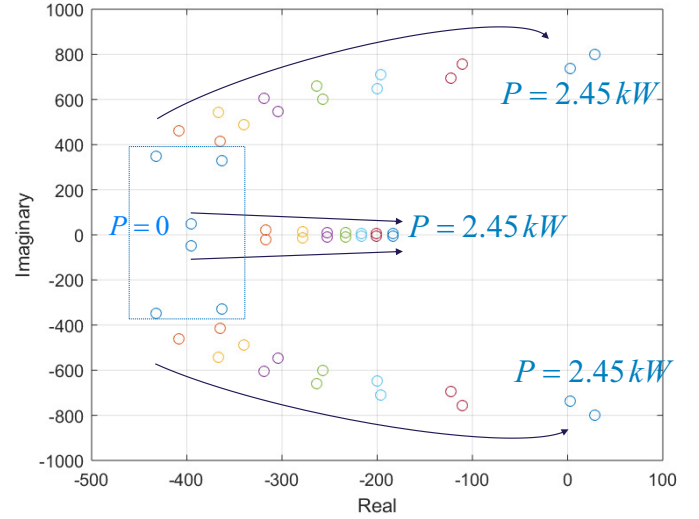Fig. 3. Phasor diagram of the voltages at PCC and grid when operating at unity power factor.

Fig. 4. Eigenvalues of the error dynamics when the real power increases from $P^* = 0$ to $P^* = 2.45$ kW and $L_g = 22$ mH.
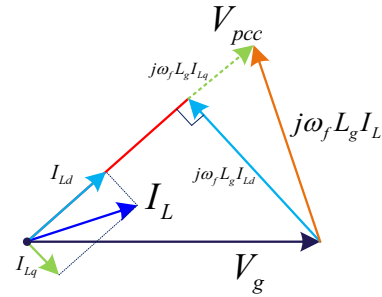
Fig. 5. Phasor diagram of the voltages at PCC and grid with consideration of reactive power [42].

$$A(x^d) = \begin{bmatrix} \frac{-R-\frac{3}{2}K_{P,p}}{L+L_g} & -\frac{L\omega_f}{L+L_g} & \frac{2\omega_c}{L+L_g}(1+\frac{K_{P,p}P^d}{V_{pcc_f}^{d2}}) & 0 & \frac{2\omega_c}{L+L_g}(\frac{K_{P,p}Q^d}{V_{pcc_f}^{d2}}) & 0 \\ \frac{L\omega_f}{L+L_g} & \frac{-R-\frac{3}{2}K_{Q,p}}{L+L_g} & -\frac{2\omega_c}{L+L_g}(\frac{K_{Q,p}Q^d}{V_{pcc_f}^{d2}}) & 0 & \frac{2\omega_c}{L+L_g}(1+\frac{K_{P,p}P^d}{V_{pcc_f}^{d2}}) & 0 \\ \frac{-R-\frac{3}{2}K_{P,p}}{L+L_g}L_g & -\frac{L\omega_f}{L+L_g}L_g & \frac{2\omega_c(1+K_{P,p}P^d/V_{pcc_f}^{d2})}{L+L_g}L_g - 2\omega_c & -\omega_0^2 & \frac{2\omega_c K_{Q,p}Q^d/V_{pcc_f}^{d2}}{L+L_g}L_g & 0 \\ 0 & 0 & 1 & 0 & 0 & 0 \\ \frac{L\omega_f}{L+L_g}L_g & \frac{-R-\frac{3}{2}K_{Q,p}}{L+L_g}L_g & -\frac{2\omega_c K_{Q,p}Q^d/V_{pcc_f}^{d2}}{L+L_g}L_g & 0 & \frac{2\omega_c(1+K_{P,p}P^d/V_{pcc_f}^{d2})}{L+L_g}L_g - 2\omega_c & -\omega_0^2 \\ 0 & 0 & 0 & 0 & 1 & 0 \end{bmatrix}. \qquad (23)$$
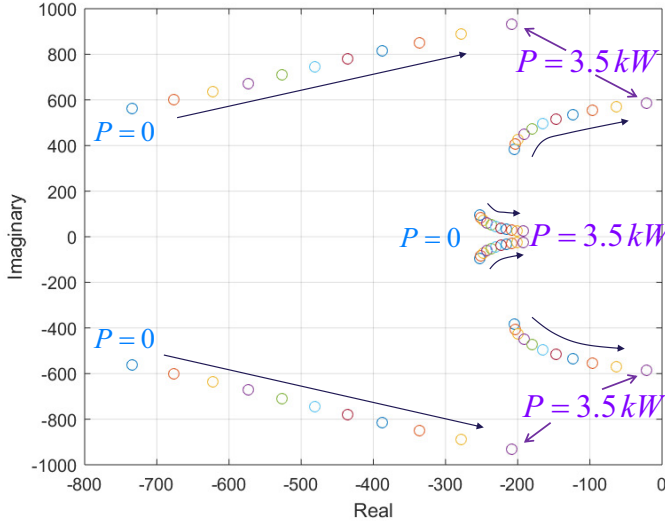
Fig. 6. Eigenvalues of the error dynamics when the real power increases from $P^d = 0$ to $P^d = 3.5\ kW$ and $Q^d = 2\ kvar$.

Fig. 7. Eigenvalues of the error dynamics when the real power increases from $P^d = 0$ to $P^d = 3.5\ kW$ and $Q^d = P^d$.

From (27), it should be noted that the following constraint should be satisfied.

$$\frac{(V_g^2 + \frac{4}{3}\omega_f L_g Q^d)^2}{4} - (\frac{2}{3}\omega_f L_g)^2(P^{d2} + Q^{d2}) \geq 0, \quad (28)$$

Thus, the amount of reactive power to be injected for stable operation could be calculated as

$$Q^d \geq \frac{(\frac{2}{3}\omega_f L_g P^d)^2 - V_g^4}{\frac{2}{3}\omega_f L_g V_g^2}. \quad (29)$$

Fig. 6 shows the eigenvalues of the closed-loop system in (22) when the real power increases from $P^d = 0$ to $P^d = 3.5$ kW, and $Q^d = 2$ kvar. In this case, the inverter could inject its rated power with the compensation of the reactive power. The eigenvalues of the closed-loop system move close to imaginary axis when the more real power is injected into the weak grid. However, all the eigenvalues are located in the left-half-plane. When $Q^d = P^d$, all the eigenvalues of the closed-loop system are also in the left-half-plane even if the VSI injects the rated power, as shown in Fig. 7. In addition, the eigenvalues move further from imaginary axis compared to $Q^d = 2$ kvar when the VSI injects its rated power. We can conclude that the VSI could inject its rated real power to the weak grid when it also injects reactive power to support the voltages at PCC.

To check the robustness to the frequency variation, we change the grid frequency from $49\ Hz$ to $51\ Hz$. In this case, we fix $P^d = 3.5\ kW$ and $Q^d = 3.5\ kvar$, as shown in Fig. 8. We can observe that the eigenvalues move to the imaginary axis but all the eigenvalues of the closed-loop system are in the left-half plane. Moreover, to check the effect of the BPF to the proposed control method, we change ζ from 0.707 to 0.1. Fig. 9(a) shows the bode plot of the BPFs with different bandwidths. We can observe that part of the eigenvalues are closer to the imaginary when ζ is decreased, as shown in Fig. 9(b). However, all the eigenvalues remain in the left-half plane when $P^d = 3.5$ kW and $Q^d = 3.5$ kvar.

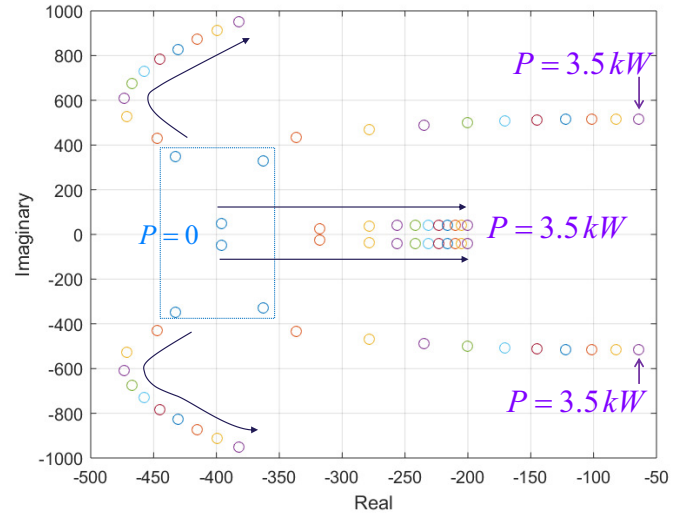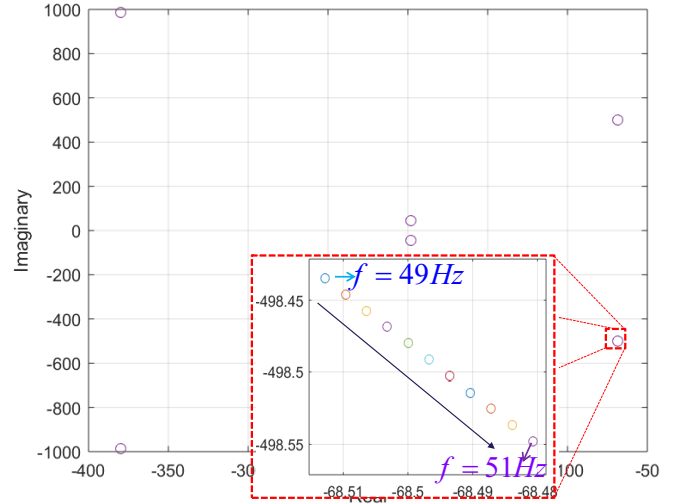Fig. 8. Eigenvalues of the error dynamics when the grid frequency is changed from 49 Hz to 51 Hz, and $P^d = 3.5$ kW and $Q^d = P^d$.

IV. PERFORMANCE VALIDATION

In this section, to validate the proposed control method, we use the MATLAB/Simulink, Simscape Power Systems and a prototype experimental setup at Aalborg University. The parameters of the system used in the simulation are listed in Table I.

A. Simulation Results

Fig. 10 shows the performance of the VSI with the proposed method when the reference of P is changed from 0.5 kW to 2 kW at 0.8 s. However, when we increase more the real power reference, the system can not be stabilized, as shown in Fig. 11. Hence, the VSI injects some certain amount of reactive power into support the PCC voltages, and it can inject its rated power 3.5 kW real power into the grid, as shown in Fig. 12.
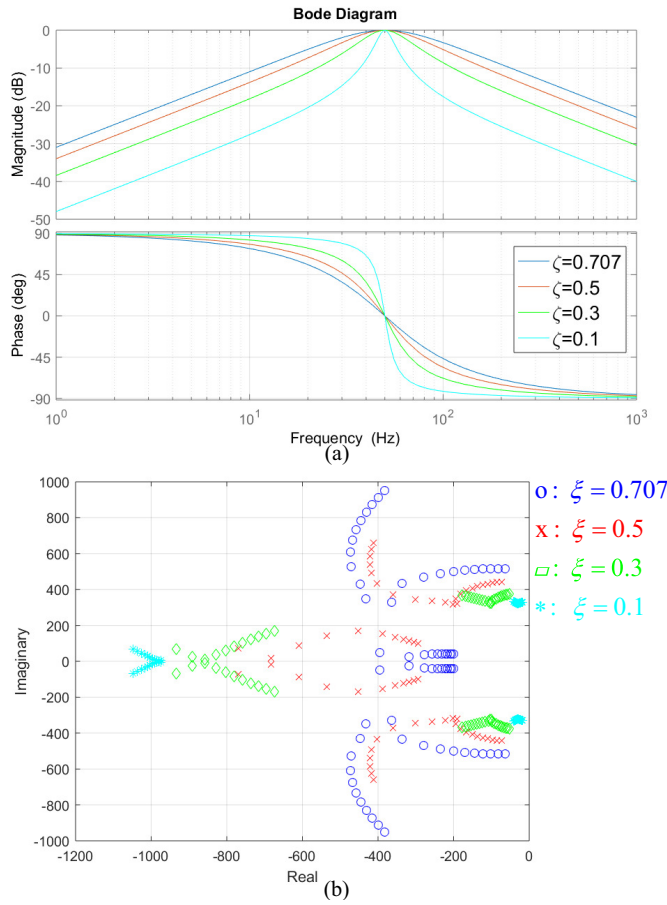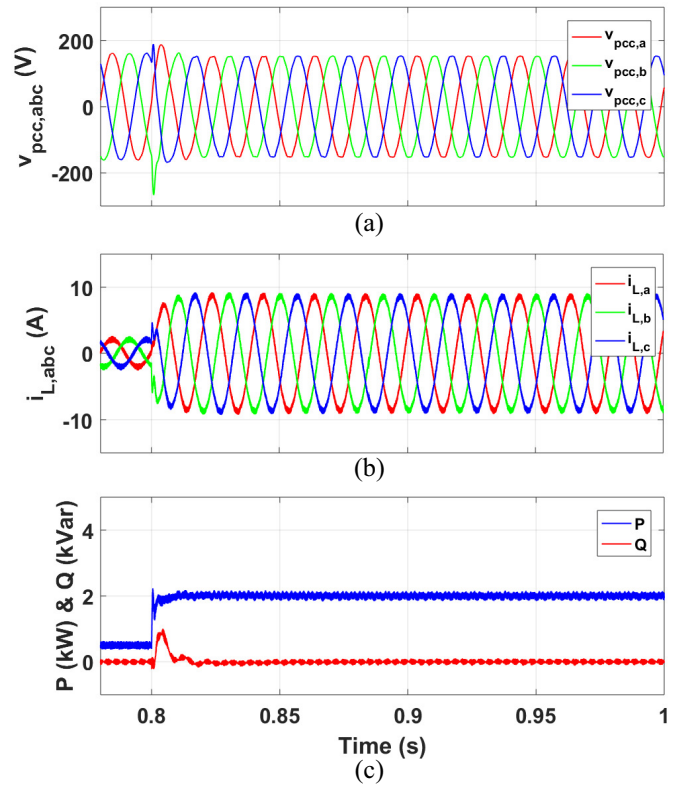
Fig. 10. Performance of the VSI with the proposed control method when the reference of P is changed from 0.5 kW to 2 kW at 0.8 s. (a) PCC voltages, (b) currents, (c) real and reactive powers.

Fig. 9. Eigenvalues of the error dynamics when the damping ratio ζ is changed from 0.707 to 0.1, and $P^d = 3.5$ kW and $Q^d = P^d$.

TABLE I
SYSTEM PARAMETERS USED IN SIMULATIONS AND EXPERIMENTS

Parameter	Symbol	Value	Unit
Nominal grid voltage	$V_{ga,rms}$	110	V
Nominal grid frequency	f	50	Hz
Dc-link voltage	V_{dc}	730	V
Filter inductance	L	6	mH
Grid inductance	L_g	22	mH
Grid capacitance	C_g	15	μF
SCR	S_{cr}	1.5	pu
Resonance bandwidth of BPF	ω_c	222	rad/s
Resonance frequency of BPF	ω_0	314	rad/s
Switching frequency	f_{sw}	10	kHz

Moreover, at 0.8 s, a converter load is connected at PCC and consumes 1.0 kW real power when the VSI regulates 3.5 kW real power and 2.0 kvar reactive power, as shown in Fig. 13. The proposed method could handle the nonlinear load as well. Once again, it is worth mentioning that the presented work is focused on the stability of grid-converter interaction under high impedance grid conditions. The steady-state harmonic (load) disturbance rejection is not the core contribution of this paper.

Fig. 14 shows the low voltage ride through capability of the proposed control method when the VSI regulates real and reactive powers to 0.5 kW and 2.0 kvar, respectively. In this case, the grid voltage has 20% sag at 0.8 s and recovers to its nominal value after 0.05 s. The proposed control method could regulate its real and reactive powers well with a small overshoot, as shown in Fig. 14(c). In this study, we did not consider the current limit to protect the VSI in the large voltage disturbance. However, the current limitation strategy could be easily implemented into the proposed control method, which has been discussed in other paper. Moreover, the reactive power requirement in the grid code is not considered as well. However, the power references could be modified based on the requirement, and it will be studied in the future.

We also test the effect of the variation of the grid frequency. As shown in Fig. 15(a), the frequency is changed from 49.5 Hz to 50.5 Hz at 0.8 s, and goes back to 49.5 Hz at 0.85 s. From Fig. 15(b), the VSI synchronizes the new frequency of
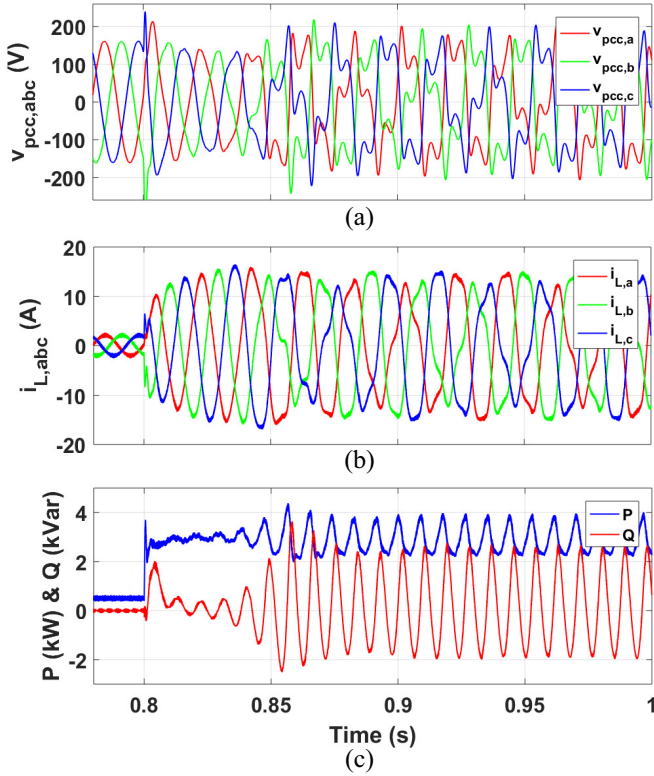
Fig. 11. Performance of the VSI with the proposed control method when the reference of P is changed from 0.5 kW to 3.5 kW at 0.8 s. (a) PCC voltages, (b) currents, (c) real and reactive powers.
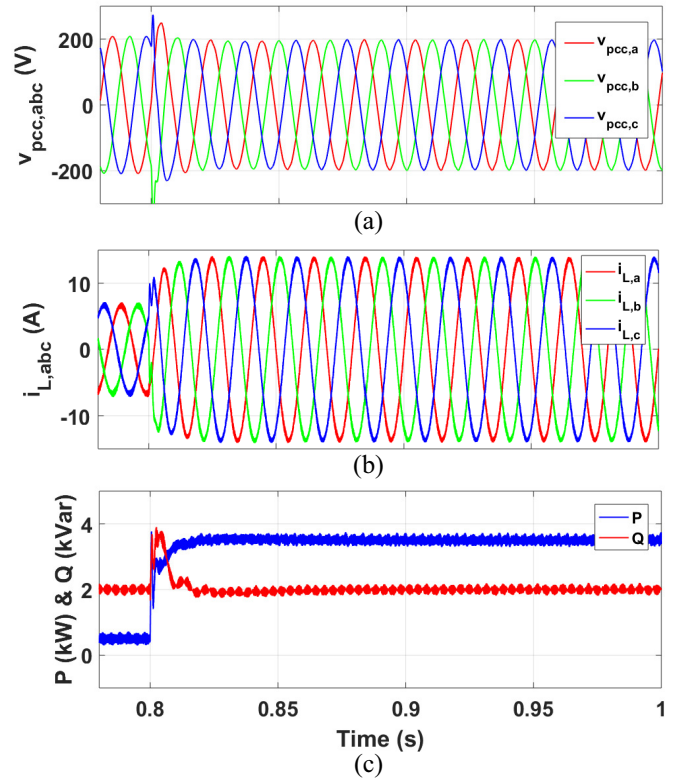

Fig. 12. Performance of the VSI with the proposed control method when the reference of P is changed from 0.5 to 3.5 kW at 0.8 s and Q is regulated to 2 kvar. (a) PCC voltages, (b) currents, (c) real and reactive powers.

the grid quickly. Hence, we can conclude that the proposed control method is robust to the variation of the grid frequency. In this case, we also use the different BPF parameter (i.e., $\zeta = 0.3$.) It can be observed that the real and reactive powers have offset when the grid frequency changes, as shown in Fig. 16. However, the steady-state power ripples are smaller than the previous ones. That means if the bandwidth of BPF is too narrow, it is not easy to handle a wide variation in grid frequency. Otherwise, it is not easy to give sufficient attenuation in higher harmonic components presented in the measured PCC voltage. It is a trade-off. In addition, we inject 5th and 7th harmonics to grid side at 0.9 s, where the THD of the grid voltage is 5.8%. When the grid voltage is distorted, the proposed method slightly increases the THD of the current from 1.2% to 2.2% in the case of $P = 3.5$ kW and $Q = 2$ kvar, as shown in Fig. 17.

B. Experimental Results

The effectiveness of the proposed method is also validated by using a prototype experimental setup. Fig. 18(a) shows a three-phase 15 kW inverter system with a 6 mH L–filter connected to a weak grid, which consists of 22 mH–L and 15 μF–C in parallel, and a grid simulator generating 110 V RMS grid voltage, as shown in Fig. 18(b). The PCC voltages and the line currents are measured by using a DS2004 A/D board, and the proposed control strategy is implemented in the DS1007 dSPACE system, where the switching pulses of the

inverter are generated by using the DS5101 digital waveform output board. In addition, a dc power supply supports a constant voltage at the dc-link. The parameters of the system used in the case study are summarized in Table I.

Fig. 19 shows the time response of the conventional VCC method when the reference of real power is changed from 0.5 kW to 2 kW. Notice that the settling time of the PLL is set to 0.05 s. As discussed in [20], the unstable phenomenon is observed when the inverter injects more real power into the grid. However, the proposed method can stabilize the system even if it injects more real power to the grid, as shown in Fig. 20. In addition, when the inverter injects more real power to the weak grid, the system becomes un stable and the protection of the system is activated, as shown in Fig. 21. This is also explaining the injected real power will affect the voltages at PCC.

Fig. 22 shows the time response of the system when the reference of real power is changed from 1.5 kW to 3 kW and the reactive power is regulated to 3 kvar. We can observe that the system is stable since the voltage is supported by the injected reactive power. Moreover, we increase the real power to its rated power 3.5 kW, as shown in Fig. 23. The inverter system is operating well with the proposed method. Consequently, we can conclude that the reactive power should also be injected when the rated real power is desired to inject into the weak grid by the inverter.
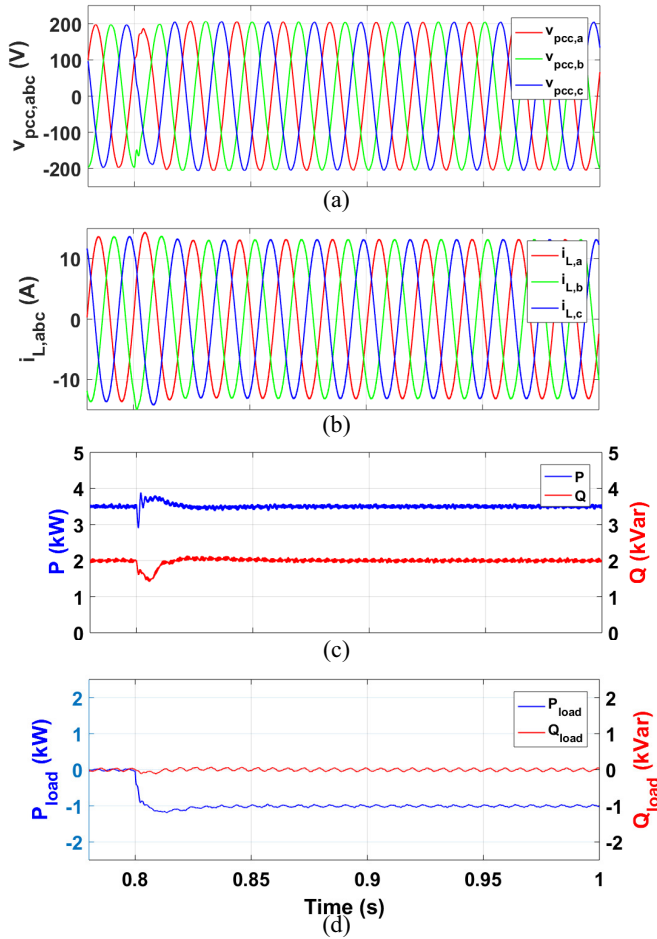
Fig. 13. Performance of the VSI when the converter load is connected at PCC. (a) PCC voltages, (b) currents, (c) real and reactive powers, (d) real and reactive powers of load.

V. CONCLUSIONS

In this paper, we have introduced a VM-DPC strategy for the three-phase VSI connected to a weak grid, where the PLL system may make the system unstable. We use a BPF for the weak grid connected VSI system to apply the concept of the GVM-DPC. From the comprehensive analysis based on the eigenvalues, the system is always stable in this operating range. In addition, in order to inject the rated real power to the weak grid, the system should generate some certain amount of reactive power to support the voltages at PCC as well. Finally, simulation and experimental results show that the proposed method is working well in the weak grid.

REFERENCES

[1] F. Blaabjerg, R. Teodorescu, M. Liserre, and A. V. Timbus, "Overview of control and grid synchronization for distributed power generation systems," *IEEE Trans. Ind. Electron.*, vol. 53, no. 5, pp. 1398–1409, 2006.

[2] F. Blaabjerg, M. Liserre, and K. Ma, "Power electronics converters for wind turbine systems," *IEEE Trans. Ind. Appl.*, vol. 48, no. 2, pp. 708–719, 2012.

[3] Y. Gui, W. Kim, and C. C. Chung, "Passivity-based control with nonlinear damping for type 2 STATCOM systems," *IEEE Trans. Power Syst.*, vol. 31, no. 4, pp. 2824–2833, 2016.
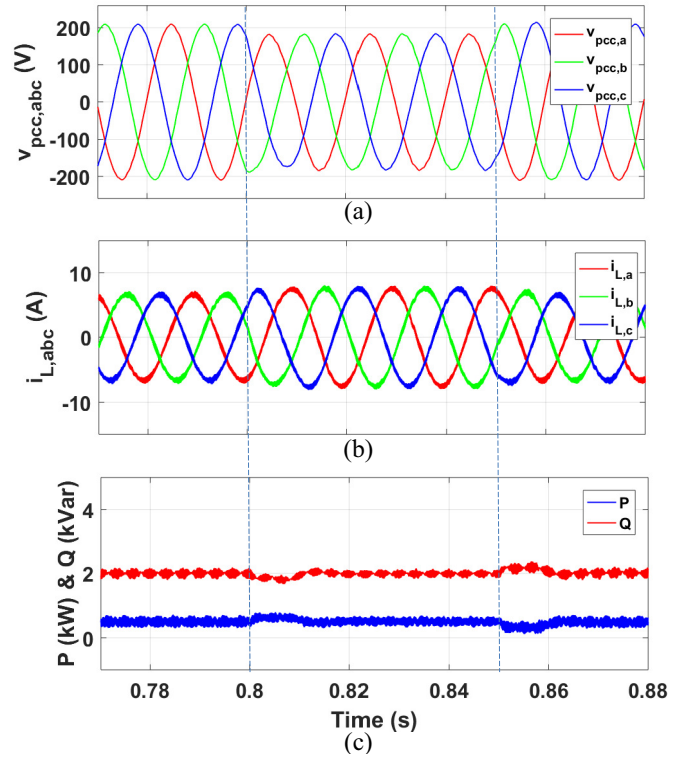
Fig. 14. Performance of the VSI with the proposed control method when the grid voltage has 20% sag at 0.8 s and recovers to its nominal value after 0.05 s. (a) PCC voltages, (b) currents, (c) real and reactive powers.
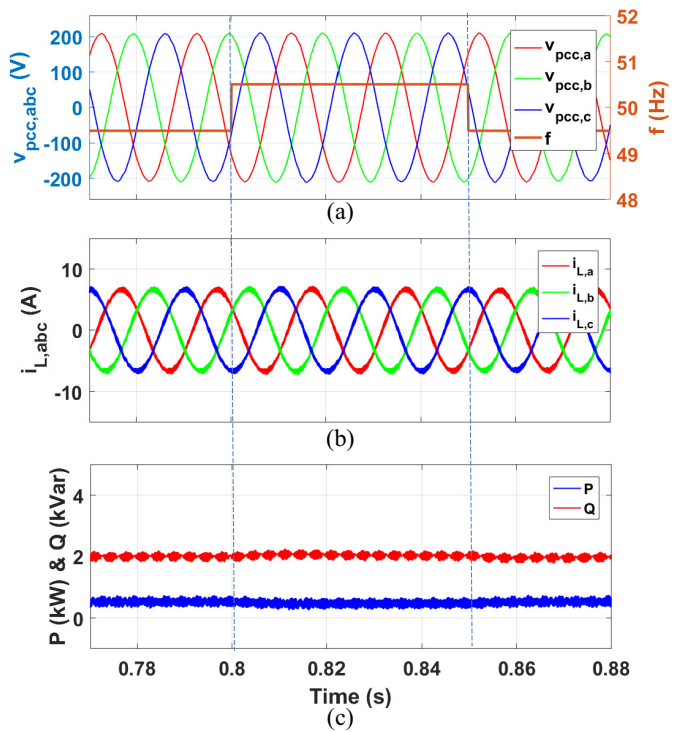

Fig. 15. Performance of the VSI when the grid frequency is changed from 49.5 Hz to 50.5 Hz. (a) PCC voltages, (b) currents, (c) real and reactive powers.
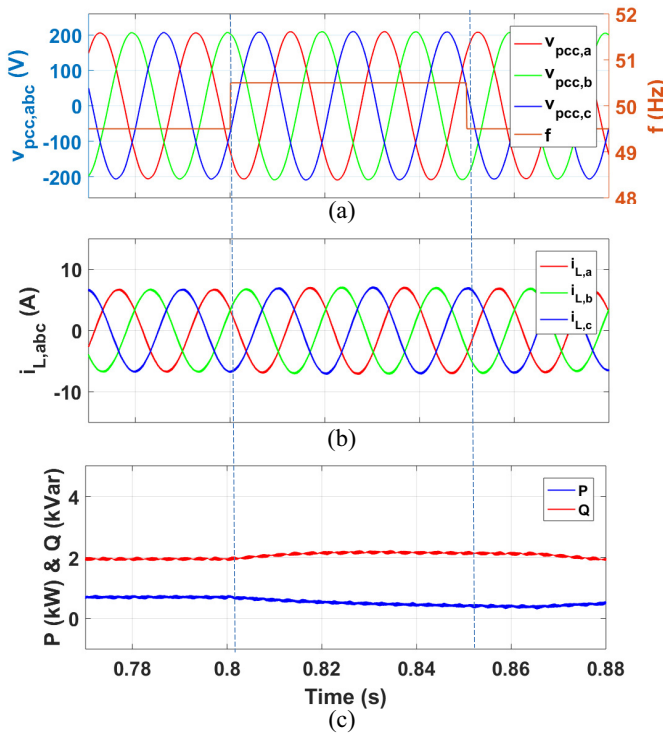
Fig. 16. Performance of the VSI with different BPF ($\zeta = 0.3$) when the grid frequency is changed from 49.5 Hz to 50.5 Hz. (a) PCC voltages, (b) currents, (c) real and reactive powers.
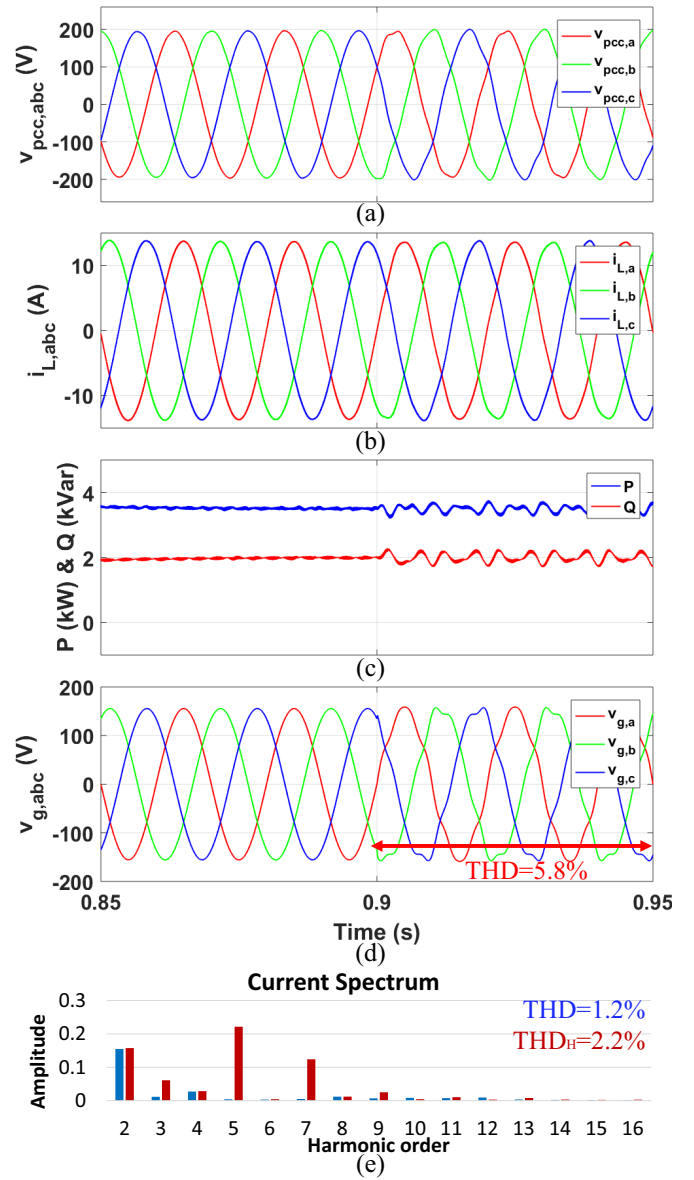

Fig. 17. Performance of the VSI when the grid voltage is distorted. (a) PCC voltages, (b) currents, (c) real and reactive powers, (d) grid voltages (THD=5.8%), (e) current spectrum.

[4] F. Blaabjerg, Y. Yang, D. Yang, and X. Wang, "Distributed power-generation systems and protection," *Proc. IEEE*, vol. 105, no. 7, pp. 1311–1331, 2017.

[5] F. Blaabjerg, *Control of Power Electronic Converters and Systems*, vol. 2. Academic Press, 2018.

[6] X. Guo, B. Wei, T. Zhu, Z. Lu, L. Tan, X. Sun, and C. Zhang, "Leakage current suppression of three-phase flying capacitor PV inverter with new carrier modulation and logic function," *IEEE Trans. Power Electron.*, vol. 33, no. 3, pp. 2127–2135, 2018.

[7] Y. Gui, B. Wei, M. Li, J. M. Guerrero, and J. C. Vasquez, "Passivity-based coordinated control for islanded AC microgrid," *Appl. Energy*, vol. 229, pp. 551–561, 2018.

[8] M. Kazmierkowski and L. Malesani, "Current control techniques for three-phase voltage-source PWM converters: a survey," *IEEE Trans. Ind. Electron.*, vol. 45, no. 5, pp. 691–703, Oct. 1998.

[9] P. Rodríguez, A. Luna, I. Candela, R. Mujal, R. Teodorescu, and F. Blaabjerg, "Multiresonant frequency-locked loop for grid synchronization of power converters under distorted grid conditions," *IEEE Trans. Ind. Electron*, vol. 58, no. 1, pp. 127–138, 2011.

[10] M. K. Ghartemani, S. A. Khajehoddin, P. K. Jain, and A. Bakhshai, "Problems of startup and phase jumps in PLL systems," *IEEE Trans. Power Electron*, vol. 27, no. 4, pp. 1830–1838, 2012.

[11] D. Dong, B. Wen, D. Boroyevich, P. Mattavelli, and Y. Xue, "Analysis of phase-locked loop low-frequency stability in three-phase grid-connected power converters considering impedance interactions," *IEEE Trans. Ind. Electron.*, vol. 62, no. 1, pp. 310–321, 2015.

[12] M. Davari and Y. A.-R. I. Mohamed, "Robust vector control of a very weak-grid-connected voltage-source converter considering the phase-locked loop dynamics," *IEEE Trans. Power Electron.*, vol. 32, no. 2, pp. 977–994, 2017.

[13] B. Kroposki, B. Johnson, Y. Zhang, V. Gevorgian, P. Denholm, B.-M. Hodge, and B. Hannegan, "Achieving a 100% renewable grid: Operating electric power systems with extremely high levels of variable renewable energy," *IEEE Power Energy Mag.*, vol. 15, no. 2, pp. 61–73, 2017.

[14] S.-K. Chung, "A phase tracking system for three phase utility interface inverters," *IEEE Trans. Power Electron.*, vol. 15, no. 3, pp. 431–438, 2000.

[15] L. Harnefors, M. Bongiorno, and S. Lundberg, "Input-admittance calculation and shaping for controlled voltage-source converters," *IEEE Trans. Ind. Electron.*, vol. 54, no. 6, pp. 3323–3334, 2007.

[16] L. Harnefors, X. Wang, A. G. Yepes, and F. Blaabjerg, "Passivity-based stability assessment of grid-connected VSCs–An overview," *IEEE J. Emerg. Sel. Topics Power Electron.*, vol. 4, no. 1, pp. 116–125, 2016.

[17] B. Wen, D. Dong, D. Boroyevich, R. Burgos, P. Mattavelli, and Z. Shen, "Impedance-based analysis of grid-synchronization stability for three-phase paralleled converters," *IEEE Trans. Power Electron.*, vol. 31, no. 1, pp. 26–38, 2016.

[18] X. Wang, L. Harnefors, and F. Blaabjerg, "Unified impedance model of grid-connected voltage-source converters," *IEEE Trans. Power Electron.*, vol. 33, no. 2, pp. 1775–1787, 2018.

[19] J. Z. Zhou, H. Ding, S. Fan, Y. Zhang, and A. M. Gole, "Impact of short-circuit ratio and phase-locked-loop parameters on the small-signal behavior of a VSC-HVDC converter," *IEEE Trans. Power Del.*, vol. 29, no. 5, pp. 2287–2296, 2014.

[20] X. Wang and F. Blaabjerg, "Harmonic stability in power electronic based power systems: Concept, modeling, and analysis," *IEEE Trans. Smart*

This article has been accepted for publication in a future issue of this journal, but has not been fully edited. Content may change prior to final publication. Citation information: DOI 10.1109/TPEL.2019.2898268, IEEE Transactions on Power Electronics
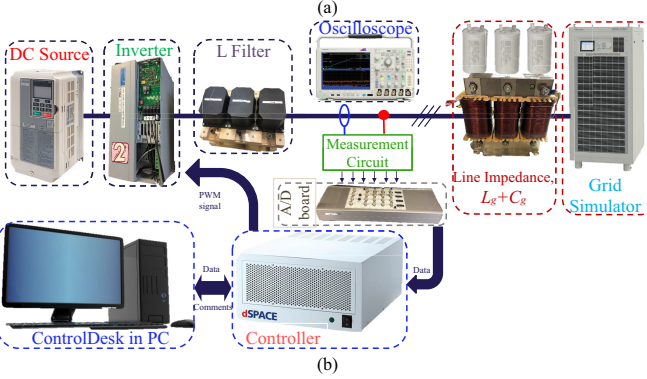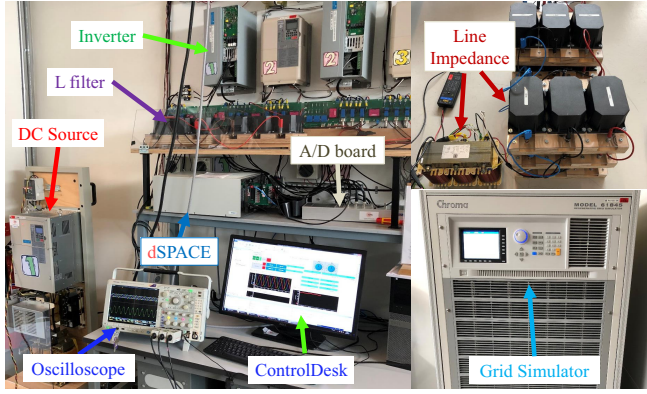
11

(a)

(b)

Fig. 18. (a) Experimental setup at Aalborg University; (b) configuration of experimental setup.
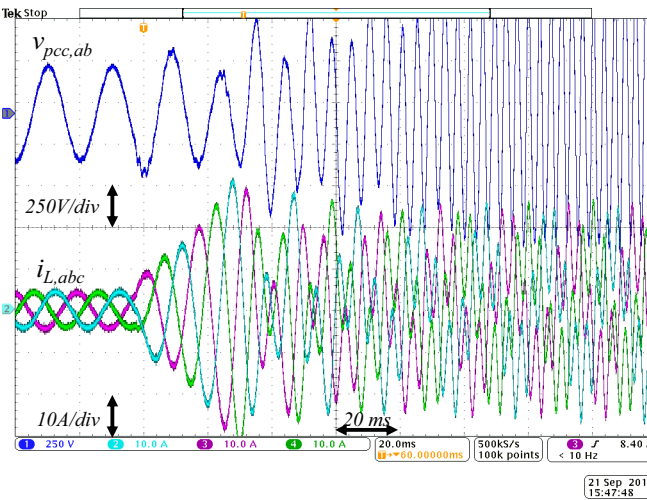

Fig. 19. Measured performance of the VSI with the conventional VCC method when the real power is changed from 0.5 kW to 2 kW. Blue: $V_{pcc,ab}$ [250 V/div]; sky blue, bubble pink, and green: $i_{L,abc}$ [10 A/div].

Fig. 20. Measured performance of the VSI with the proposed control method when the real power is changed from 0.5 kW to 2 kW. Blue: $V_{pcc,ab}$ [250 V/div]; sky blue, bubble pink, and green: $i_{L,abc}$ [10 A/div].

Fig. 21. Measured performance of the VSI with the proposed control method when the real power is changed from 0.5 kW to 3 kW. Blue: $V_{pcc,ab}$ [250 V/div]; sky blue, bubble pink, and green: $i_{L,abc}$ [10 A/div].
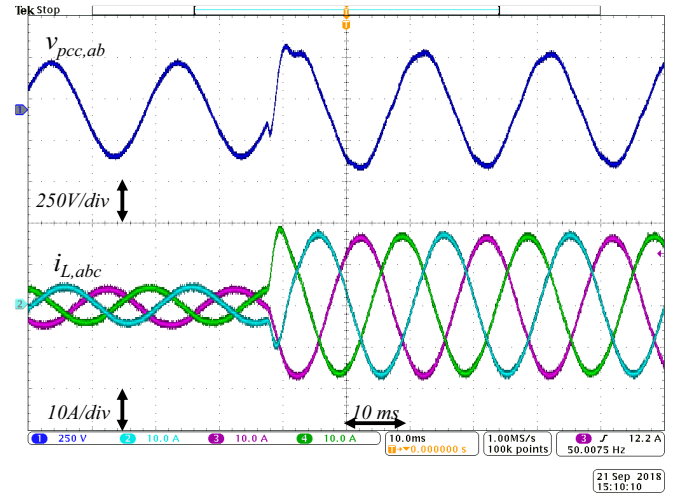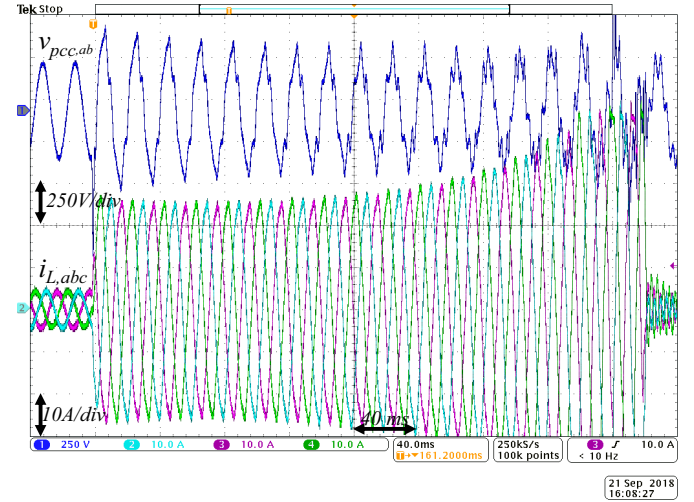
Grid, 2018, in press, DOI: 10.1109/TSG.2018.2812712.

[21] N. Bottrell, M. Prodanovic, and T. C. Green, "Dynamic stability of a microgrid with an active load," *IEEE Trans. Power Electron.*, vol. 28, no. 11, pp. 5107–5119, 2013.

[22] X. Wang, F. Blaabjerg, and P. C. Loh, "Passivity-based stability analysis and damping injection for multiparalleled VSCs with LCL filters," *IEEE Trans. Power Electron.*, vol. 32, no. 11, pp. 8922–8935, 2017.

[23] L. Harnefors, R. Finger, X. Wang, H. Bai, and F. Blaabjerg, "Vsc input-admittance modeling and analysis above the Nyquist frequency for passivity-based stability assessment," *IEEE Trans. Ind. Electron.*, vol. 64, no. 8, pp. 6362–6370, 2017.

[24] T. Noguchi, H. Tomiki, S. Kondo, and I. Takahashi, "Direct power control of PWM converter without power-source voltage sensors," *IEEE Trans. Ind. Appl.*, vol. 34, no. 3, pp. 473–479, 1998.

[25] M. Malinowski, M. Jasiński, and M. P. Kazmierkowski, "Simple direct power control of three-phase PWM rectifier using space-vector modulation (DPC-SVM)," *IEEE Trans. Ind. Electron.*, vol. 51, no. 2, pp. 447–454, 2004.

[26] A. Bouafia, J.-P. Gaubert, and F. Krim, "Predictive direct power control

This article has been accepted for publication in a future issue of this journal, but has not been fully edited. Content may change prior to final publication. Citation information: DOI 10.1109/TPEL.2019.2898268, IEEE Transactions on Power Electronics
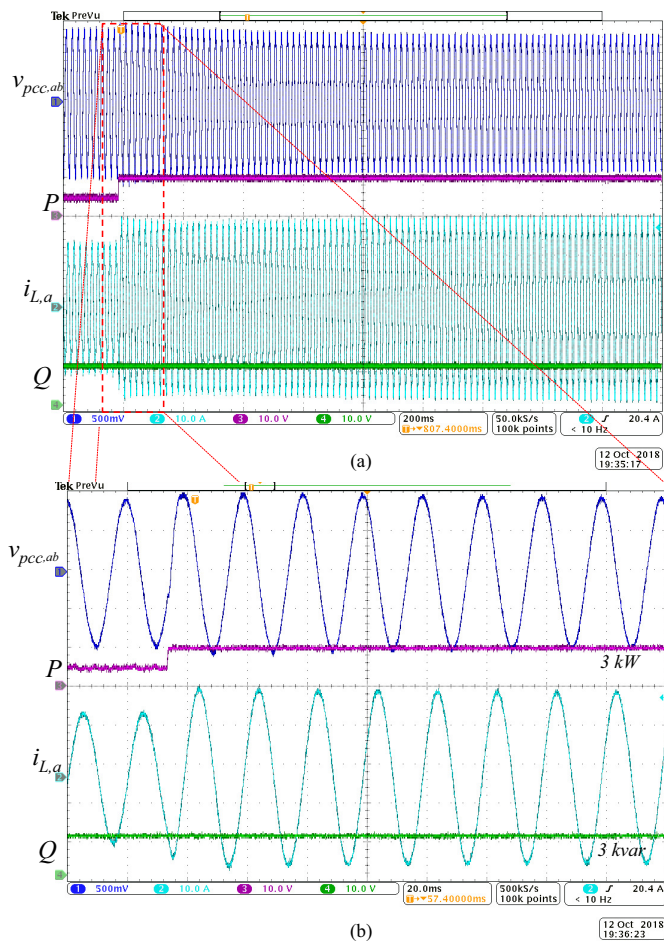
12

Fig. 22. Measured performance of the VSI with the proposed control method when it injects 3.0 kW and 3.0 kvar to the grid. Blue: $V_{pcc,ab}$ [250 V/div]; sky blue: $i_{L,a}$ [10 A/div]; bubble pink: P [3 kW/div]; green: Q [3 kvar/div].
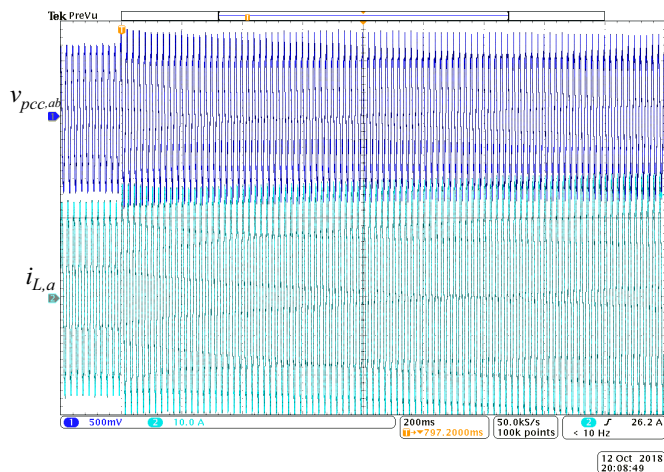

Fig. 23. Measured performance of the VSI with the proposed control method when it injects 3.5 kW with 3.5 kvar to the grid. Blue: $V_{pcc,ab}$ [250 V/div]; sky blue: $i_{L,a}$ [10 A/div].
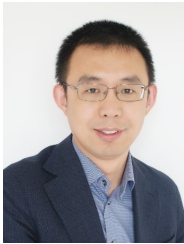
of three-phase pulsewidth modulation (PWM) rectifier using space-vector modulation (SVM)," *IEEE Trans. Power Electron.*, vol. 25, no. 1, pp. 228–236, 2010.

[27] D. Zhi and L. Xu, "Direct power control of DFIG with constant switching frequency and improved transient performance," *IEEE Trans. Energy Convers.*, vol. 22, no. 1, pp. 110–118, 2007.

[28] S. Vazquez, J. A. Sanchez, J. M. Carrasco, J. I. Leon, and E. Galvan, "A model-based direct power control for three-phase power converters," *IEEE Trans. Ind. Electron.*, vol. 55, no. 4, pp. 1647–1657, 2008.

[29] J. Hu, L. Shang, Y. He, and Z. Zhu, "Direct active and reactive power regulation of grid-connected DC/AC converters using sliding mode control approach," *IEEE Trans. Power Electron.*, vol. 26, no. 1, pp. 210–222, 2011.

[30] Y. Gui, G. H. Lee, C. Kim, and C. C. Chung, "Direct power control of grid connected voltage source inverters using port-controlled Hamiltonian system," *Int. J. Control Autom. Syst.*, vol. 15, no. 5, pp. 2053–2062, 2017.

[31] S. Larrinaga, M. Vidal, E. Oyarbide, and J. Apraiz, "Predictive control strategy for DC/AC converters based on direct power control," *IEEE Trans. Ind. Electron.*, vol. 54, no. 3, pp. 1261–1271, 2007.

[32] P. Antoniewicz and M. P. Kazmierkowski, "Virtual-flux-based predictive direct power control of AC/DC converters with online inductance estimation," *IEEE Trans. Ind. Electron.*, vol. 55, no. 12, pp. 4381–4390, 2008.

[33] Z. Song, W. Chen, and C. Xia, "Predictive direct power control for three-phase grid-connected converters without sector information and voltage vector selection," *IEEE Trans. Power Electron.*, vol. 29, no. 10, pp. 5518–5531, 2014.

[34] D.-K. Choi and K.-B. Lee, "Dynamic performance improvement of AC/DC converter using model predictive direct power control with finite control set," *IEEE Trans. Ind. Electron.*, vol. 62, no. 2, pp. 757–767, 2015.

[35] S. Vazquez, A. Marquez, R. Aguilera, D. Quevedo, J. I. Leon, and L. G. Franquelo, "Predictive optimal switching sequence direct power control for grid-connected power converters," *IEEE Trans. Ind. Electron.*, vol. 62, no. 4, pp. 2010–2020, 2015.

[36] Y. Gui, C. Kim, and C. C. Chung, "Grid voltage modulated direct power control for grid connected voltage source inverters," in *Amer. Control Conf.*, pp. 2078–2084, 2017.

[37] Y. Gui, C. Kim, C. C. Chung, J. M. Guerrero, Y. Guan, and J. C. Vasquez, "Improved direct power control for grid-connected voltage source converters," *IEEE Trans. Ind. Electron.*, vol. 65, no. 10, Oct. 2018.

[38] Y. Gui, M. Li, J. Lu, S. Golestan, J. M. Guerrero, and J. C. Vasquez, "A voltage modulated DPC approach for three-phase PWM rectifier," *IEEE Trans. Ind. Electron.*, vol. 65, no. 10, pp. 7612–7619, Oct. 2018.

[39] Y. Gui, X. Wang, and F. Blaabjerg, "Vector current control derived from direct power control for grid-connected inverters," *IEEE Trans. Power Electron.*, DOI 10.1109/TPEL.2018.2883507, pp. 1–1, 2018.

[40] H. Akagi, E. H. Watanabe, and M. Aredes, *The instantaneous power theory*. Wiley Online Library, 2007.

[41] F. Z. Peng and J.-S. Lai, "Generalized instantaneous reactive power theory for three-phase power systems," *IEEE Trans. Instrum. Meas.*, vol. 45, no. 1, pp. 293–297, 1996.

[42] D. Yang, X. Wang, F. Liu, K. Xin, Y. Liu, and F. Blaabjerg, "Adaptive reactive power control of PV power plants for improved power transfer capability under ultra-weak grid conditions," *IEEE Trans. Smart Grid*, 2018, in press, DOI: 10.1109/TSG.2017.2762332.
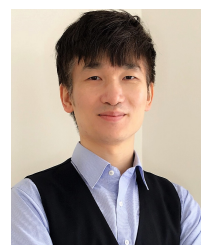
Yonghao Gui (S'11-M'17) was born in Shenyang, China. He received the B.S. degree in automation from Northeastern University, Shenyang, China, in 2009, and the M.S. and Ph.D. degrees in electrical engineering from Hanyang University, Seoul, South Korea, in 2012 and 2017, respectively.

From February 2017 to November 2018, he worked with the Department of Energy Technology, Aalborg University, Aalborg, Denmark, as a Postdoctoral Researcher. Since December 2018, he has been working with the Automation & Control Section, Department of Electronic Systems, Aalborg University, Aalborg, Denmark, where he is currently an Assistant Professor. His research interests include control of power electronics in power systems, Energy Internet, and Smart Grids.

Dr. Gui is a member of the IEEE Power and Energy Society, the IEEE Control System Society, the IEEE Power Electronics Society, and the IEEE Industrial Electronics Society.
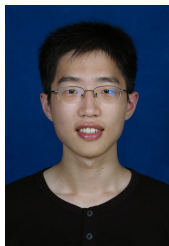
This article has been accepted for publication in a future issue of this journal, but has not been fully edited. Content may change prior to final publication. Citation information: DOI 10.1109/TPEL.2019.2898268, IEEE Transactions on Power Electronics

13

Xiongfei Wang (S'10-M'13-SM'17) received the B.S. degree from Yanshan University, Qinhuangdao, China, in 2006, the M.S. degree from Harbin Institute of Technology, Harbin, China, in 2008, both in electrical engineering, and the Ph.D. degree in energy technology from Aalborg University, Aalborg, Denmark, in 2013.

Since 2009, he has been with the Department of Energy Technology, Aalborg University, where he became Assistant Professor in 2014, an Associate Professor in 2016, a Professor and Research Program Leader for Electronic Power Grid Infrastructure in 2018. His current research interests include modeling and control of grid-interactive power converters, stability and power quality of power electronic based power systems, active and passive filters.

Dr. Wang serves as an Associate Editor for the IEEE TRANSACTIONS ON POWER ELECTRONICS, the IEEE TRANSACTIONS ON INDUSTRY APPLICATIONS, and the IEEE JOURNAL OF EMERGING AND SELECTED TOPICS IN POWER ELECTRONICS. He was selected into Aalborg University Strategic Talent Management Program in 2016. He received six IEEE prize paper awards, the outstanding reviewer award of IEEE TRANSACTIONS ON POWER ELECTRONICS in 2017, and the IEEE PELS Richard M. Bass Outstanding Young Power Electronics Engineer Award in 2018.

Frede Blaabjerg (S'86-M'88-SM'97-F'03) was with ABB-Scandia, Randers, Denmark, from 1987 to 1988. From 1988 to 1992, he got the PhD degree in Electrical Engineering at Aalborg University in 1995. He became an Assistant Professor in 1992, an Associate Professor in 1996, and a Full Professor of power electronics and drives in 1998. From 2017 he became a Villum Investigator. He is honoris causa at University Politehnica Timisoara (UPT), Romania and Tallinn Technical University (TTU) in Estonia.

His current research interests include power electronics and its applications such as in wind turbines, PV systems, reliability, harmonics and adjustable speed drives. He has published more than 600 journal papers in the fields of power electronics and its applications. He is the co-author of four monographs and editor of ten books in power electronics and its applications.

He has received 30 IEEE Prize Paper Awards, the IEEE PELS Distinguished Service Award in 2009, the EPE-PEMC Council Award in 2010, the IEEE William E. Newell Power Electronics Award 2014 and the Villum Kann Rasmussen Research Award 2014. He was the Editor-in-Chief of the IEEE TRANSACTIONS ON POWER ELECTRONICS from 2006 to 2012. He has been Distinguished Lecturer for the IEEE Power Electronics Society from 2005 to 2007 and for the IEEE Industry Applications Society from 2010 to 2011 as well as 2017 to 2018. In 2019-2020 he serves a President of IEEE Power Electronics Society. He is Vice-President of the Danish Academy of Technical Sciences too.

He is nominated in 2014-2018 by Thomson Reuters to be between the most 250 cited researchers in Engineering in the world.

Heng Wu (S'10-M'13-S'17) received the B.S. degree in electrical engineering and automation and the M.S. degree in power electronic engineering both from Nanjing University of Aeronautics and Astronautics (NUAA), Nanjing, China, in 2012 and 2015, respectively. From 2015 to 2017, He was an Electrical Engineer with NR Electric Co., Ltd, Nanjing, China. He is currently working toward the Ph.D. degree in power electronic engineering in Aalborg University, Aalborg, Denmark. His research interests include the modelling and stability analysis of the power electronic based power systems.